Supplementary Material (ESI) for New Journal of Chemistry

SUPPLEMENTARY INFORMATION

Complexation of 6-(4'-(toluidinyl)naphthalene-2-sulphonate by β-cyclodextrin and linked β-cyclodextrin dimers

Duc-Truc Pham,[a] Philip Clements,[a] Christopher J. Easton,[b] John Papageorgiou,[a] Bruce L. May,[a] and Stephen F. Lincoln[a]*

[a]*School of Chemistry and Physics, University of Adelaide, South Australia, 5005, Australia*
[b]*Research School of Chemistry, Australian National University, Canberra, ACT 0200, Australia*

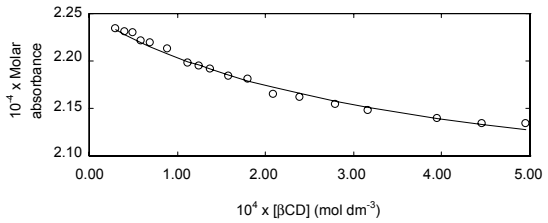

Fig. S1. Absorbance variation of TNS^- with $[\beta CD]_{total}$ at 265 nm under the same conditions as in Fig. 3 in the main text. The solid curve represents the best fit obtained over the range 250-275 and 310-330 nm.

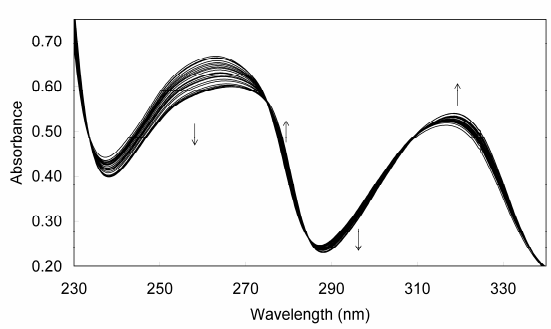

Fig. S2. UV-vis absorption changes by TNS^- (3.00×10^{-5} mol dm^{-3}) with $[66\beta CD_2su]_{total}$ in the range 0, 4.00 and 8.10×10^{-6}, 1.23, 1.62, 1.99, 2.39, 2.76, 3.16, 3.55,4.50, 4.98, 5.52, 6.36, 7.21, 8.41 and 9.60×10^{-5}, 1.12, 1.27, 1.43, 1.59, 1.79 and 1.98×10^{-5} mol dm^{-3}. The arrows indicate the direction of absorbance change as $[66\beta CD_2su]_{total}$ increases. Isosbestic points occur at 233.5, 275, 284.5 and 308.25 nm.

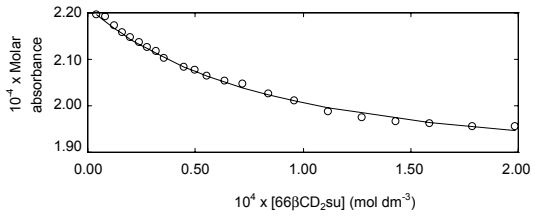

Fig. S3. Absorbance variation of TNS^- with $[66\beta CD_2su]_{total}$ at 260 nm under the same conditions as in Fig. S2. The solid curve represents the best fit obtained over the ranges 235-275 nm.

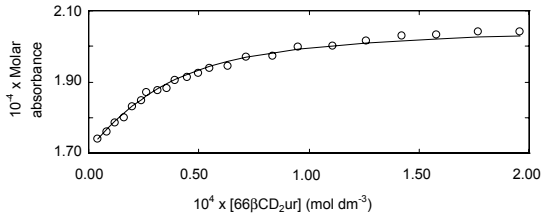

Fig. S4. Absorbance variation of TNS^- with $[66\beta CD_2ur]_{total}$ at 320 nm under the same conditions as in Fig. 4 in the main text. The solid curve represents the best fit obtained over the ranges 235-270 and 310-335 nm.

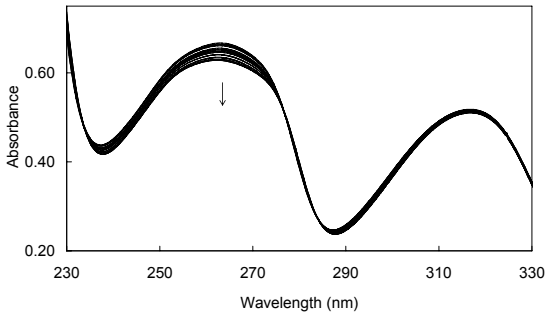

Fig. S5. UV-vis absorption changes at 298.2 K shown by TNS^- (3.00×10^{-5} mol dm^{-3}) with $[36\beta CD_2su]_{total}$ in the range 0, 5.08, and 7.58×1.0^{-6}, and 1.01, 1.50, 2.22, 2.47, 2.81, 3.14, 3.52, 4.01, 4.51, 5.24, 5.98, 6.96, 7.96, 8.95, and 9.89×1.0^{-5}, and 1.11 and 1.24×10^{-4} mol dm^{-3}. The arrows indicate the direction of absorbance change as $[36\beta CD_2su]_{total}$ increases. Isosbestic points occur at 233.5, 277.0, and 383.5 nm.

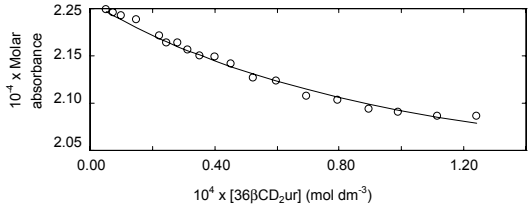

Fig. S6. Absorbance variation of TNS^- with $[36\beta CD_2su]_{total}$ at 260 nm under the same conditions as in Fig. S5. The solid curve represents the best fit obtained over the range 240-270 nm.

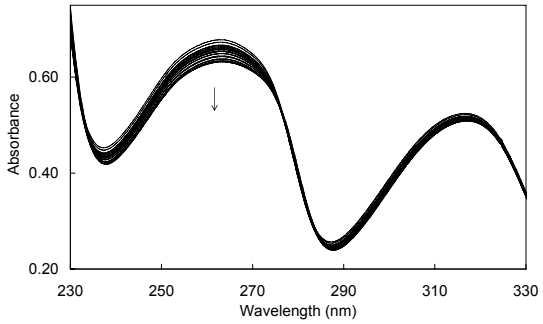

Fig. S7. UV-vis absorption changes at 298.2 K shown by TNS^- (3.00×10^{-5} mol dm^{-3}) with $[33\beta CD_2su]_{total}$ in the range 0, 5.00×1.0^{-6}, and 1.01, 1.25, 1.50, 1.74, 1.97, 2.22, 2.48, 2.79, 3.11, 3.53, 4.00, 4.49, 5.25, 5.97, 6.95, 7.96, 89, and 9.89×1.0^{-5}, and 1.11 and 1.23×10^{-4} mol dm^{-3}. The arrows indicate the direction of absorbance change as $[36\beta CD_2su]_{total}$ increases. An isosbestic point occurs at 233.5 nm.

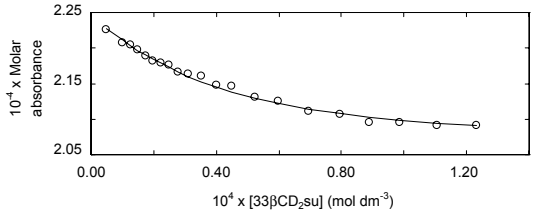

Fig. S8. Absorbance variation of TNS^- with $[33\beta CD_2su]_{total}$ at 260 nm under the same conditions as in Fig. S7. The solid curve represents the best fit obtained over the range 240-270 nm.

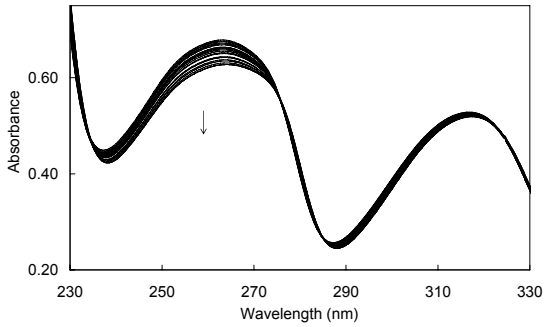

Fig. S9. UV-vis absorption changes at 298.2 K shown by TNS^- (3.00×10^{-5} mol dm^{-3}) with $[36\beta CD_2ur]_{total}$ in the range 0, 2.50, 5.05 and 7.53×1.0^{-6}, and 1.00, 1.25, 1.51, 1.74, 1.99, 2.24, 2.47, 2.79, 3.12, 3.46, 4.51, 5.24, 5.97, 6.93, 7.93 and 9.88×1.0^{-5}, and 1.11 and 1.23 $\times 10^{-4}$ mol dm^{-3}. The arrows indicate the direction of absorbance change as $[36\beta CD_2ur]_{total}$ increases. Isosbestic points occur at 234.0, 276.0 and 284.5 nm.

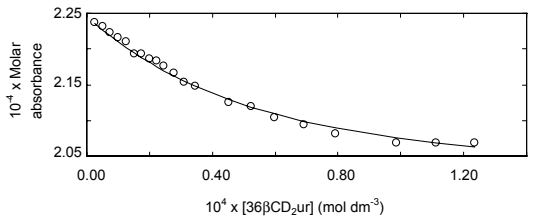

Fig. S10. Absorbance variation of TNS^- with $[36\beta CD_2ur]_{total}$ at 260 nm under the same conditions as in Fig. S9. The solid curve represents the best fit obtained over the range 235-275 nm.

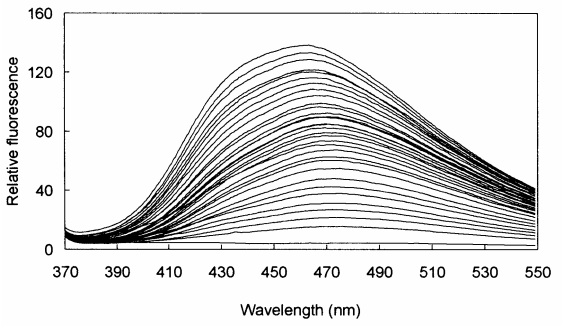

Fig. S11. Increase in the relative fluorescence of TNS^- (1.00×10^{-6} mol dm^{-3}) with $[\beta CD]_{total}$ in the range 0, 4.35 and 7.50×10^{-5}, and 1.07, 1.34, 1.79, 2.27, 2.97, 3.83, 4.82, 5.51, 6.50, 7.62, 8.76 and 9.98×10^{-4} and 1.11, 1.22, 1.37, 1.50, 1.68, 1.86, 2.06, 2.38, 2.72, 3.15, 3.60, 4.05, 4.50, 4.96, 5.40, 6.03, 6.75 and 7.49 mol dm^{-3}. The excitation wavelength was 320 nm.

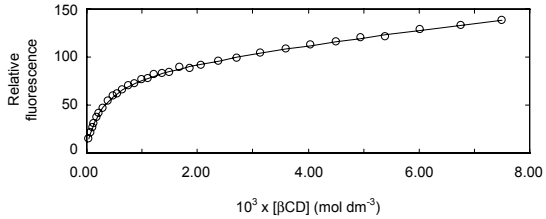

Fig. S12. The relative fluorescence increase of TNS^- with $[\beta CD]_{total}$ at 463 nm under the same conditions as in Fig. S11. The solid curve represents the best fit obtained over the range 400-500 nm.

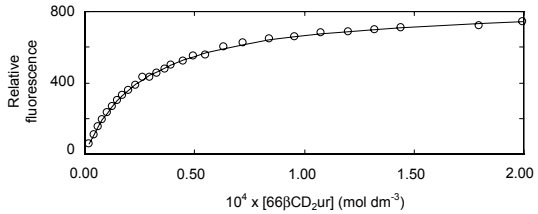

Fig. S13. The relative fluorescence increase of TNS^- with $[66\beta CD_2ur]_{total}$ at 435 nm under the same conditions as in Fig. 5 in the text. The solid curve represents the best fit obtained over the range 400-500 nm.

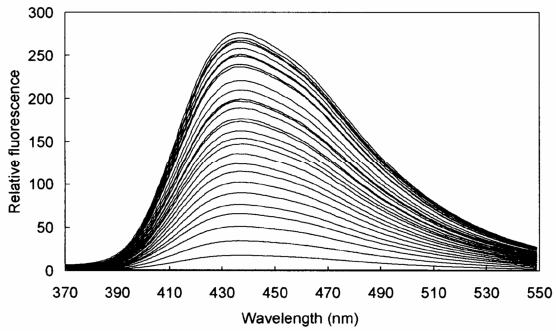

Fig. S14. Increase in the relative fluorescence of TNS^- (1.00×10^{-6} mol dm^{-3}) in with $[66\beta CD_2su]_{total}$ in the range 0, 4.60 and 9.40×10^{-6}, and 1.48, 2.10, 2.47, 3.09, 3.73, 4.42, 5.04, 5.83, 6.61, 7.39, 8.22 and 9.10×10^{-5}, and 1.00,1.12, 1.24, 1.37, 1.58, 1.80, 2.10, 2.40, 2.70, 3.00, 3.30, 3.61, 4.01, 4.50 and 5.00×10^{-4} mol dm^{-3}. The excitation wavelength was 320 nm.

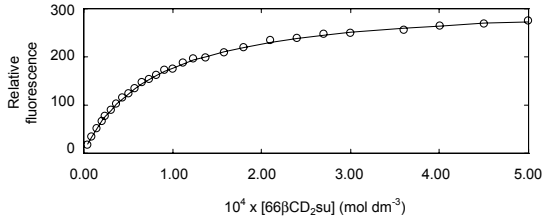

Fig. S15. Relative fluorescence increase of TNS^- with $[66\beta CD_2su]_{total}$ at 440 nm under the same conditions as in Fig. S14. The solid curve represents the best fit obtained over the range 400-500 nm.

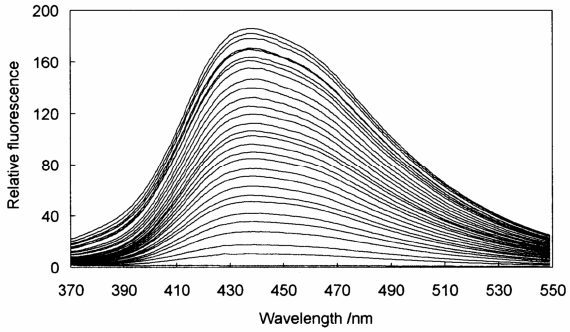

Fig. S16. Increase in the relative fluorescence of TNS^- (1.00×10^{-6} mol dm^{-3}) with $[36\beta CD_2su]_{total}$ in the range 0, 4.90 and 9.80×10^{-6}, and 1.45, 2.01, 2.47, 3.08, 3.66, 4.26, 4.97, 5.75, 6.55, 7.33, 8.17, 9.16 and 9.96×10^{-5}, and 1.12, 1.24, 1.37, 1.58, 1.81, 2.11, 2.41, 2.70, 3.00, 3.30, 3.60, 4.00, 4.51 and 5.00×10^{-4} mol dm^{-3}. The excitation wavelength was 320 nm.

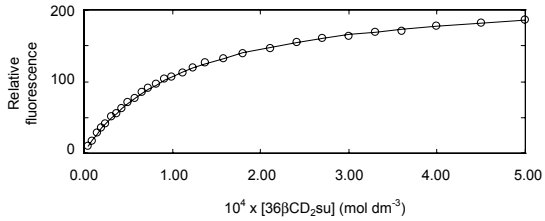

Fig. S17. Relative fluorescence increase of TNS^- with $[36\beta CD_2su]_{total}$ at 440 nm under the same conditions as in Fig. S16. The solid curve represents the best fit obtained over the range 400-500 nm.

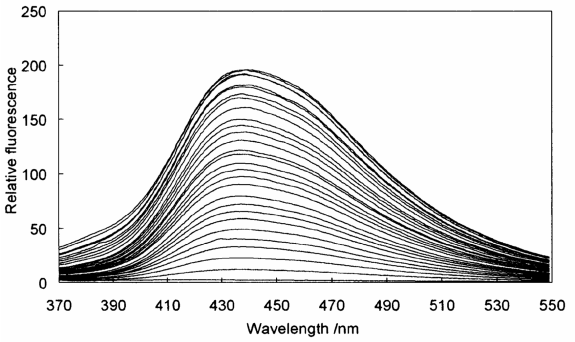

Fig. S18. Increase in the relative fluorescence of TNS^- (1.00×10^{-6} mol dm^{-3}) with $[33\beta CD_2su]_{total}$ in the range 0, 4.80 and 9.80×10^{-6}, and 1.51, 2.02, 2.53, 3.12, 3.74, 4.23, 4.98, 5.86, 6.58, 7.40, 8.20, and 9.13×10^{-5}, and 1.12, 1.24, 1.38, 1.50, 1.82, 2.11, 2.42, 2.73, 3.02, 3.32, 3.63, 4.51 and 5.02×10^{-4} mol dm^{-3}. The excitation wavelength was 320 nm.

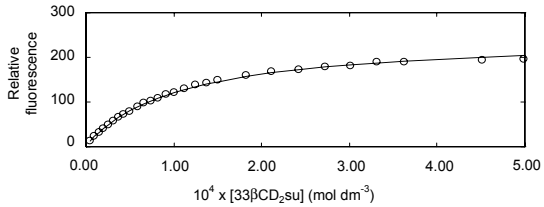

Fig. S19. Relative fluorescence increase of TNS^- with $[33\beta CD_2su]_{total}$ at 440 nm under the same conditions as in Fig. S18. The solid curve represents the best fit obtained over the range 400-500 nm.

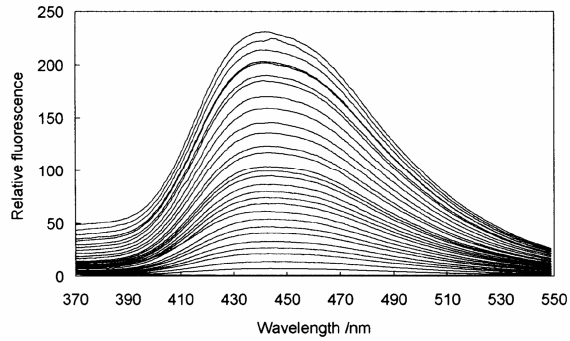

Fig. S20. Increase in the relative fluorescence of TNS^- (1.00×10^{-6} mol dm^{-3}) with $[36\beta CD_2ur]_{total}$ in the range 0, 2.00, 4.04, 6.12, 8.08, and 9.96×10^{-6}, and 1.28, 1.48, 1.75, 2.02, 2.35, 2.64, 2.96, 3.28, 3.64, 3.99, 4.47, 4.97, 5.52, 6.38, 7.20, 8.42, and 9.65×10^{-5}, and 1.20,1.32, 1.44, 1.61, 1.81, and 2.00×10^{-4} mol dm^{-3}. The excitation wavelength was 320 nm.

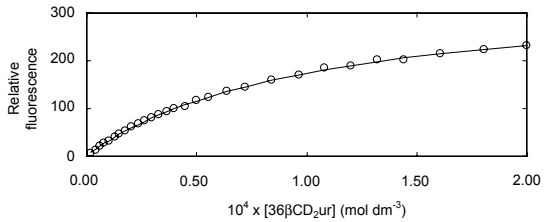

Fig. S21. Relative fluorescence increase of TNS^- with $[36\beta CD_2ur]_{total}$ at 440 nm under the same conditions as in Fig. S21. The solid curve represents the best fit obtained over the range 400-500 nm.

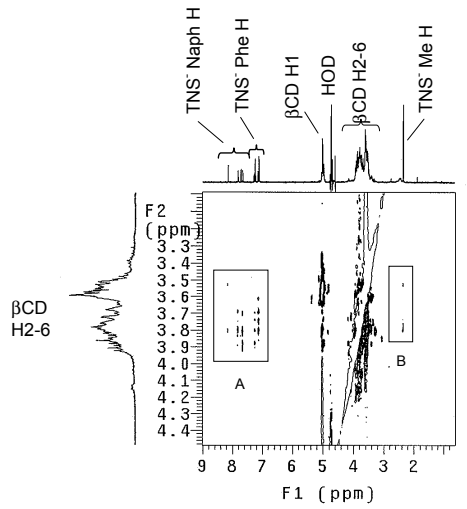

Fig. S22. 2D ^1H ROESY NMR (600 MHz) spectrum of a D_2O solution equimolar at 2.00×10^{-3} mol dm^{-3} in TNS^- and $36\beta CD_2su$. The rectangles drawn on the spectrum, A and B, contain the cross-peaks arising from the NOE interactions between the annular H3, H5 and H6 protons of $36\beta CD_2su$ and the aromatic and methyl protons of TNS^-, respectively.

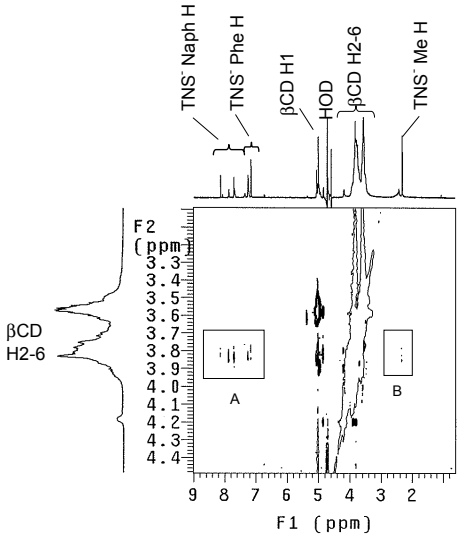

Fig. S23. 2D ^{1}H ROESY NMR (600 MHz) spectrum of a D_2O solution equimolar at 2.00 × 10^{-3} mol dm^{-3} in TNS^- and 33βCD_2su. The rectangles drawn on the spectrum, A and B, contain the cross-peaks arising from the NOE interactions between the annular H3, H5 and H6 protons of 33βCD_2su and the aromatic and methyl protons of TNS^-, respectively.

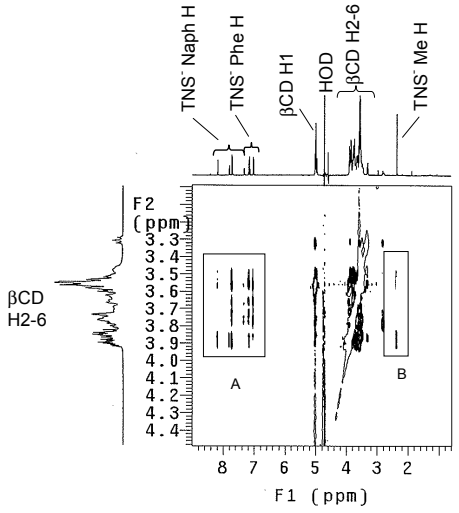

Fig. S24. 2D ^{1}H ROESY NMR (600 MHz) spectrum of a D_2O solution equimolar at 2.00 × 10^{-3} mol dm^{-3} in TNS^- and 66βCD_2ur. The rectangles drawn on the spectrum, A and B, contain the cross-peaks arising from the NOE interactions between the annular H3, H5 and H6 protons of 66βCD_2ur and the aromatic and methyl protons of TNS^-, respectively.

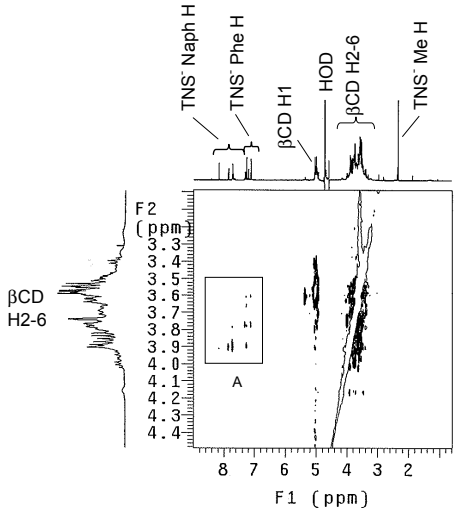

Fig. S25. 2D ^{1}H ROESY NMR (600 MHz) spectrum of a D_2O solution equimolar at 2.00 × 10^{-3} mol dm^{-3} in TNS^- and 36βCD_2ur. The rectangles drawn on the spectrum, A and B, contain the cross-peaks arising from the NOE interactions between the annular H3, H5 and H6 protons of 36βCD_2ur and the aromatic protons of TNS^-.

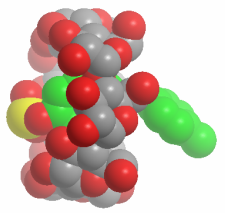

Fig. S26. The energy minimized β$CD.TNS^-$ model structure of one of four possible isomers. The carbons of TNS^- are shown in green for clarity.

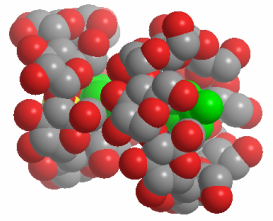

Fig. S27. The energy minimized β$CD_2.TNS^-$ model structure of one of four possible isomers. The carbons of TNS^- are shown in green for clarity.

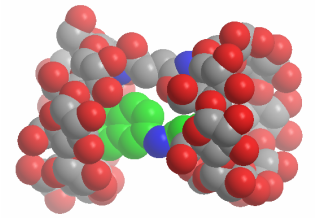

Fig. S28. The energy minimized 36βCDsu.TNS$^-$ model structure of one of two possible isomers. The carbons of TNS$^-$ are shown in green for clarity.

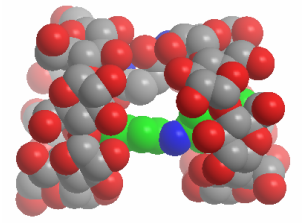

Fig. S29. The energy minimized 33βCDsu.TNS$^-$ model structure. The carbons of TNS$^-$ are shown in green for clarity.

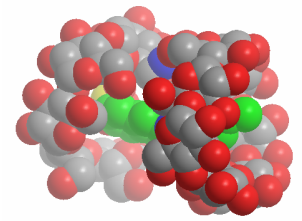

Fig. S30. The energy minimized 66βCDur.TNS$^-$ model structure. The carbons of TNS$^-$ are shown in green for clarity.

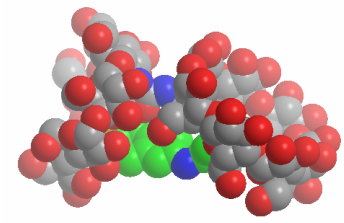

Fig. S31. The energy minimized 36βCDsu.TNS$^-$ model structure of one of two possible isomers. The carbons of TNS$^-$ are shown in green for clarity.

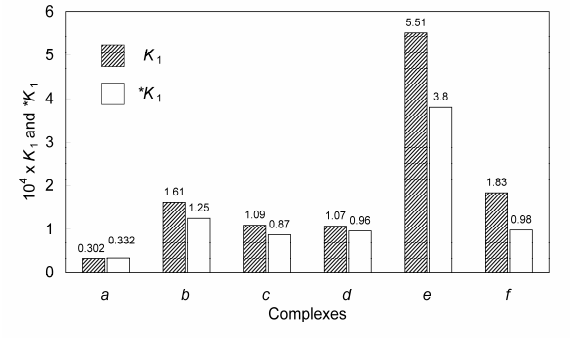

Fig. 32. The similar relative trends in K_1 and $^*K_1$ for complexatation of TNS^- by *a*) βCD, *b*) 66βCD$_2$su, *c*) 36βCD$_2$su, *d*) 33βCD$_2$su, *e*) 66βCD$_2$ur, and *f*) 36βCD$_2$ur.

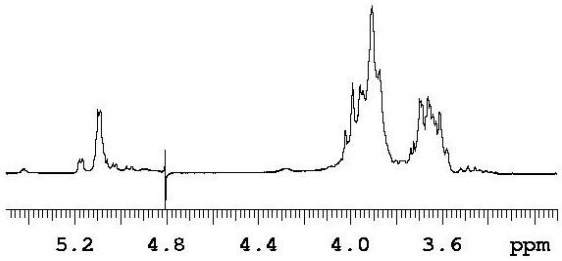

Figure S33. ^{1}H NMR (300 MHz) spectrum of 36βCD$_2$ur in D$_2$O solution.

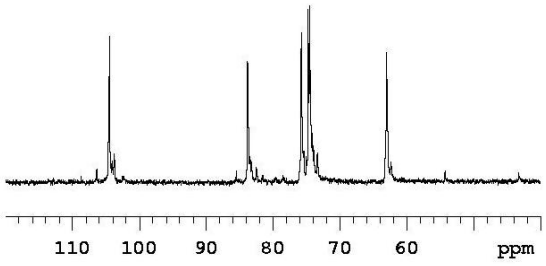

Figure S34. ^{13}C NMR (300 MHz) spectrum of 36βCD$_2$ur in D$_2$O solution.